# Cloud cavitation behaviour on a hydrofoil due to fluid-structure interaction

Samuel Smith[1]*, James Venning[1], Dean Giosio[1], Paul Brandner[1], Bryce Pearce[1], Yin Lu Young[2]

ISROMAC 2017

International Symposium on Transport Phenomena and Dynamics of Rotating Machinery

Maui, Hawaii

December 16-21, 2017

**Abstract**

Despite recent extensive research into fluid-structure interaction (FSI) of cavitating hydrofoils there remains insufficient experimental data to explain many of these observed phenomena. The cloud cavitation behaviour around a hydrofoil due to the effect of FSI is investigated utilizing rigid and compliant 3D hydrofoils held in a cantilevered configuration in a cavitation tunnel. The hydrofoils have identical undeformed geometry of tapered planform with constant NACA0009 section. The rigid model is made of stainless steel and the compliant model of carbon and glass fibre reinforced epoxy resin with the structural fibres aligned along the span-wise direction to avoid material bend-twist coupling. Tests were conducted at an incidence of 6°, a mean chord based Reynolds Number of $0.7 \times 10^6$, and cavitation number of 0.8. Force measurements were simultaneously acquired with high-speed imaging to enable correlation of forces with tip bending deformations and cavity physics. Hydrofoil compliance was seen to dampen the higher frequency force fluctuations while showing strong correlation between normal force and tip deflection. The 3D nature of the flow field was seen to cause complex cavitation behaviour with two shedding modes observed on both models.

**Keywords**

Cavitation — Fluid-Structure Interaction — Hydrofoil

[1] *Cavitation Research Laboratory, Australian Maritime College, Launceston, Australia*

[2] *Department of Naval Architecture and Marine Engineering, University of Michigan, Ann Arbour, MI, USA*

*__Corresponding author__: ssmith18@utas.edu.au

## INTRODUCTION

The FSI characteristics of flow over a lifting body can significantly effect the performance of maritime propulsion and control systems. Recent research into the development of composite propellers[1, 2] and active control surfaces [3] has taken place to exploit the ability to passively tailor geometric aspects of the hydrofoil such as skew and pitch based on the loading distribution [4]. Not only does this self-adaptive behaviour give the ability to design a more energy efficient propeller, but also delay and mitigate the adverse effects of cavitation. One of these effects is the unsteady loading and induced vibration due to the shedding of cloud cavitation.

The effect of unsteady cloud cavitation on the hydroelastic response of hydrofoils has previously been investigated [5, 6, 7, 8, 9, 10], with recently Pearce et al. [11] showing that the cavity dynamics can influence the FSI response. In addition to the classical shed vortex induced structural response in single phase flow, there is interaction between the development of cavitation on the structural dynamics [9, 8]. These effects are highlighted in experiments by Akcabay et al. [6] where increased hydrofoil flexibility was seen to increase the cavity length as well as cause a reduction in the cloud cavitation shedding frequency. Further research also shows that flexibility broadens the induced vibration frequency content potentially leading to severe vibration amplification caused by lock-in [6]. Increased vibrations also occur when the unsteady cavity closure approaches the hydrofoil trailing edge due to high amplitude load fluctuations caused by periodic shedding of sheet-cloud cavitation. In these investigations into the effect of cloud cavitation on hydroelastic response, there is limited discussion on changes in the cavitation pattern and shedding mechanisms due to the hydroelastic response.

Sheet and cloud cavitation was first extensively studied by Knapp [12] observing the detachment/shedding of cloud cavitation from a sheet cavity. Since then, several mechanisms have been identified as the primary instability causing periodic shedding depending on the condition. These included growth of interfacial instabilities such as Kelvin-Helmholtz waves [13, 14], re-entrant jet formation [15, 16, 17, 18, 19, 20] and shock propagation [21, 22, 23]. In a recent study on cloud cavitation about a sphere, all three mechanisms have been observed occuring either under varying flow conditions or as a complex coupled mechanism [24].

To reduce the complexity of the cavitation dynamics, much research into hydrofoil cloud cavitation has focused on 2D flows to limit 3D effects and span-wise variations as shown in Figure 1. This is highlighted in time resolved PIV experiments on a 3D hydrofoil by Foeth et al. [25] showing significant cavitation stability sensitivity to 3D flow effects. Span-wise variations are still observed on 2D hydrofoils where the span-wise cavity length is seen to be proportional to the stream-wise length [26]. This relationship can result in span-wise cavity lengths that are compatible with the hydrofoil geometry. In these instances, the shedding cloud cavitation exhibits much stronger periodicity than in other conditions [17].

Force and tip displacement measurements are presented

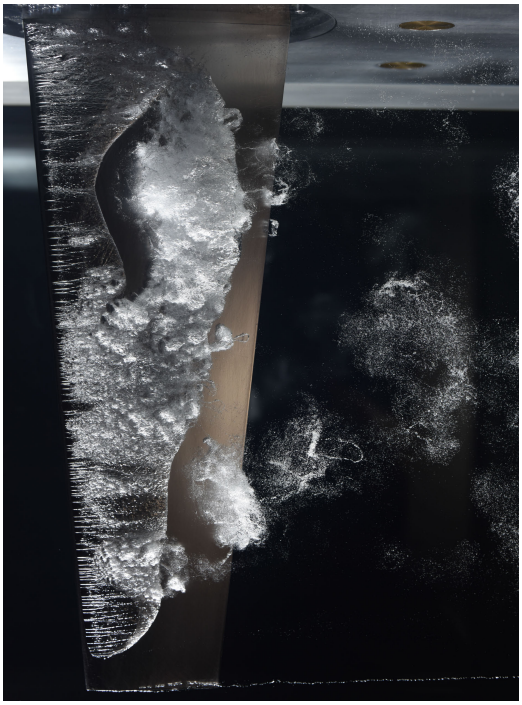

**Figure 1.** Cavitation about a NACA 0009 stainless steel hydrofoil at $\sigma = 0.8$, $Re_c = 0.7 \times 10^6$ and $\alpha = 6°$.

for a nominally rigid stainless steel and flexible composite hydrofoil experiencing cloud cavitation. Synchronised high speed photography is used to analyse the cavitation behaviour and assess the correlation between the cavity dynamics and forces experienced. The aim of this research is to further the understanding of cloud cavitation about a 3D hydrofoil and how FSI can influence its behaviour.

## EXPERIMENTAL OVERVIEW

### Model Hydrofoil Details

Geometry and mechanical properties of the hydrofoil models has been selected based on modelling the static and dynamic fluid-structure interaction typical of propellers and control surfaces. The chosen geometry was a symmetric (unswept) trapezoidal planform of 300 mm span with a 60 mm tip and 120 mm root chord, providing an aspect ratio = 3.33. The chord length was chosen to be compatible with the mounting to the water tunnel test section and to achieve a chord based Reynolds number $Re_c = 0.7 \times 10^6$. The unswept geometry, in conjunction with a span-wise alignment of the fibre orientation, was intentionally chosen to principally consider bending deformation only of the flexible hydrofoil. A modified NACA0009 section profile with a thicker trailing edge was selected for improved manufacture of the flexible composite model (see Zarruk et al [27] for further details).

The flexible (composite) model was manufactured as a carbon/glass-epoxy hybrid structure consisting of a polyolefin scaffold core, T700 unidirectional carbon fibre and biaxial E-glass fabric used as the key structural components with an outermost fine E-glass basket weave layer to aid surface finish. A full lay-up sequence and construction procedure is detailed in [27] where the composite hydrofoil model used in the present study is termed the CFRP00 hydrofoil. The rigid (stainless steel) model was machined from a Type 316 stainless steel billet with both models manufactured to ±0.1 mm surface tolerance and 0.8 μm surface finish.

The response spectrum of both hydrofoils was determined from both numerical simulations and digital image correlation experiments [28] with results summarized in Table 1. First mode natural frequencies were obtained in air at 93 Hz and 120 Hz, and in water at 54 and 45 Hz for the stainless steel (rigid) and composite (flexible) models respectively.

| Hydrofoil Dynamic Properties | Hydrofoil | |
|---|---|---|
| | Rigid | Flexible |
| First bending mode in air (Hz) | 93 | 120 |
| First bending mode in water (Hz) | 54 | 45 |
| Second bending mode in air (Hz) | 379 | 428 |
| Second bending mode in water (Hz) | 259 | 186 |

**Table 1.** Hydrofoil natural frequencies obtained from numerical simulations and experiments [28].

### Experimental Setup

Measurements were carried out in the Cavitation Research Laboratory (CRL) water tunnel at the Australian Maritime College. The tunnel test section is 0.6 m square by 2.6 m long in which the operating velocity and pressure ranges are 2 to 12 m/s and 4 to 400 kPa absolute respectively. The tunnel volume is 365 $m^3$ with demineralised water (conductivity of order 1 μS/cm). The test section velocity is measured from one of two (high and low range) Siemens Sitransp differential pressure transducers models 7MF4433-1DA02-2AB1-Z and 7MF4433-1FA02-2AB1-Z (measuring the calibrated contraction differential pressure) with estimated precisions of 0.007 and 0.018 m/s respectively. A detailed description of the facility is given in [29]. As shown in Figure 2, two profiled plates are used to clamp the model within a housing that is attached to a 6-component force balance. The hydrofoil, located at the mid length of the test section, extends vertically into the flow through a 160 mm diameter penetration in the ceiling. The penetration is made fair (to 50 μm) using a disk mounted, in this case, on the measurement side of the balance. The fairing disk has a 0.5 mm radial clearance to avoid interference with the force measurement.

### Experimental Techniques

Data was obtained for a cavitation number of 0.8 at a Reynolds number (based on mean chord length) of $0.7 \times 10^6$ with the models at an incidence of 6°. The cavitation number is defined as $\sigma = 2(p - p_v)/\rho U_\infty^2$ and Reynolds number as $Re = U_\infty c/\nu$, where $p$ is the static pressure at the test section centreline, $p_v$ is the vapour pressure, $\rho$ is the water density, $U_\infty$ is the test section velocity, $c$ is the mean chord and $\nu$ is the kinematic viscosity of the water. Of the total load vector measured,

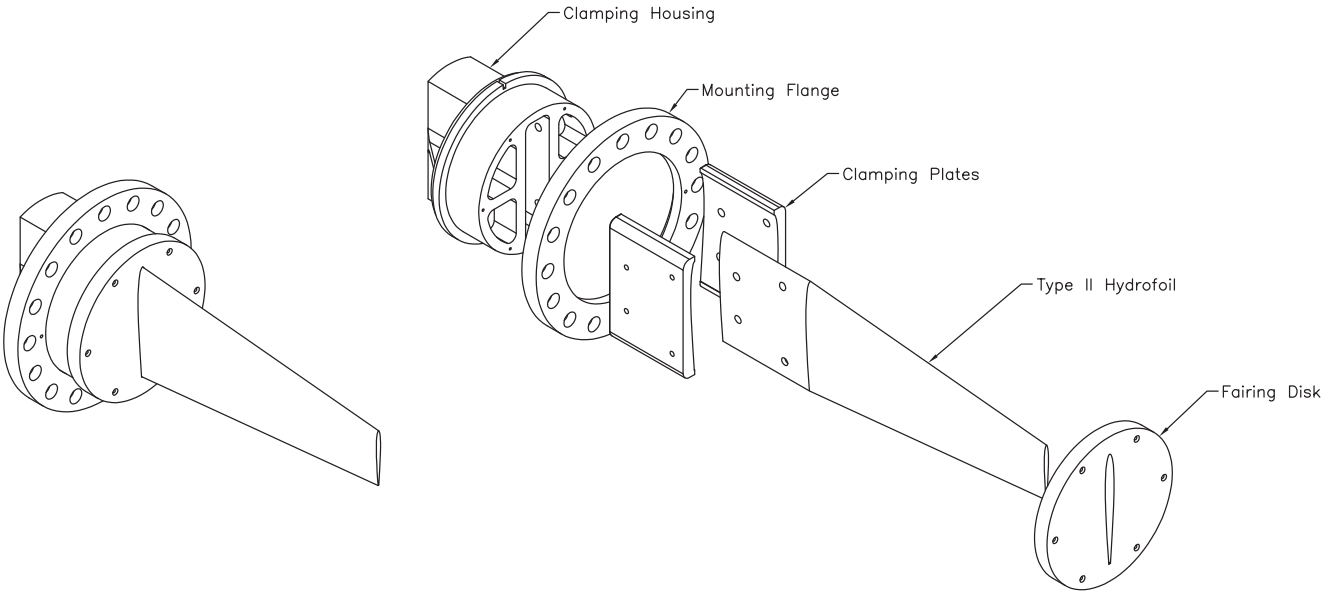


**Figure 2.** Hydrofoil model assembly showing an exploded view of the clamping housing arrangement allowing continuity of the reinforcing fibres for the CFRP models.

only the time-varying component of the normal force is presented. The force balance was calibrated by a least squares fit between a basis vector loading cycle and the 6 outputs giving a $6 \times 6$ matrix. An estimated precision on all components is less than 0.1%.

The cavitation behaviour was recorded using high speed photography with a HighSpeedStar8 (LaVision, Germany) mounted on the side of the test section. The camera was outfitted with a Nikkor f/1.4 50 mm lens and setup with a magnification factor of 3.28 px/mm. High speed images were recorded with a spatial resolution of $1024 \times 1024$ at 7,000 Hz for the rigid hydrofoil where the flexible foil was recorded at 1,000 Hz due to data acquisition limits.

A previous study [27] has shown the stainless steel model to be nominally rigid with a maximum tip deflection of less than 5% of the mean chord compared with 15% for the composite model. The force data for the stainless steel model was found to be nominally invariant with Reynolds number for $\alpha \leq 6°$. On this basis, tip bending displacement, $\delta_{tip}$, was only recorded for the flexible model with measurements achieved by tracking 2.3 mm diameter white dots on the tip of the hydrofoil. Further information on the technique used in similar experiments can be found in [30]. This was achieved using a HighSpeedStar5 high speed camera mounted on the bottom of the test section. The camera was outfitted with a Nikkor f/1.4 105 mm lens where images had a magnification factor of 13.38 px/mm. Images were recorded at 1,000 Hz with a spatial resolution of $512 \times 1024$.

The high speed photography was synchronized with the force measurement acquisition by simultaneous triggering from a BNC Model 575 Pulse Generator. Force and tunnel flow data were sampled at 7,000 Hz and 1,000 Hz, respectively.

## RESULTS AND DISCUSSION

### Force and Tip Displacement Time Series

The measured normal force, $X$, is presented as a dimensionless coefficient, $C_X = 2X/(\rho A U_\infty^2)$, where $A$ denotes the planform area. The frequency content of the $X$ force experienced by either hydrofoil shows a common primary frequency at approximately 37 Hz with secondary frequencies at 49 and 42 HZ for the rigid and flexible hydrofoils, respectively (Figure 3). The rigid hydrofoil exhibits significantly greater amplitude at both the primary and secondary frequencies.

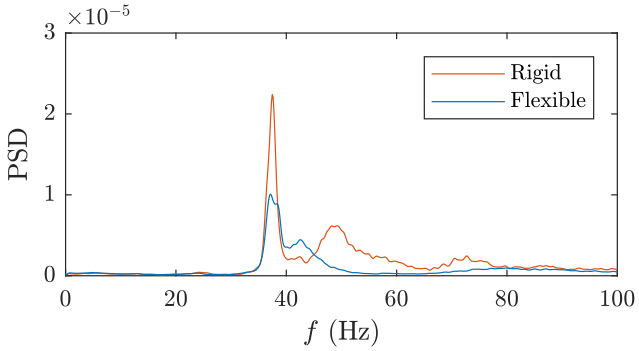


**Figure 3.** Narrowband $X$ force power spectral density (PSD) for the rigid and flexible hydrofoils at $\sigma = 0.8$, $Re_c = 0.7 \times 10^6$ and $\alpha = 6°$.

Figure 4 shows a short time series of $C_X$, the unsteady tip bending displacement to chord ratio, $\delta'_{tip}/c$, and pixel intensity, $I$, for both the rigid and flexible hydrofoils. Pixel intensity was taken along the span, $s$, at $0.24s$, $0.47s$ and $0.77s$ from the root and at 75% of the chord at those positions for both hydrofoils. Frames taken from the synchronised high

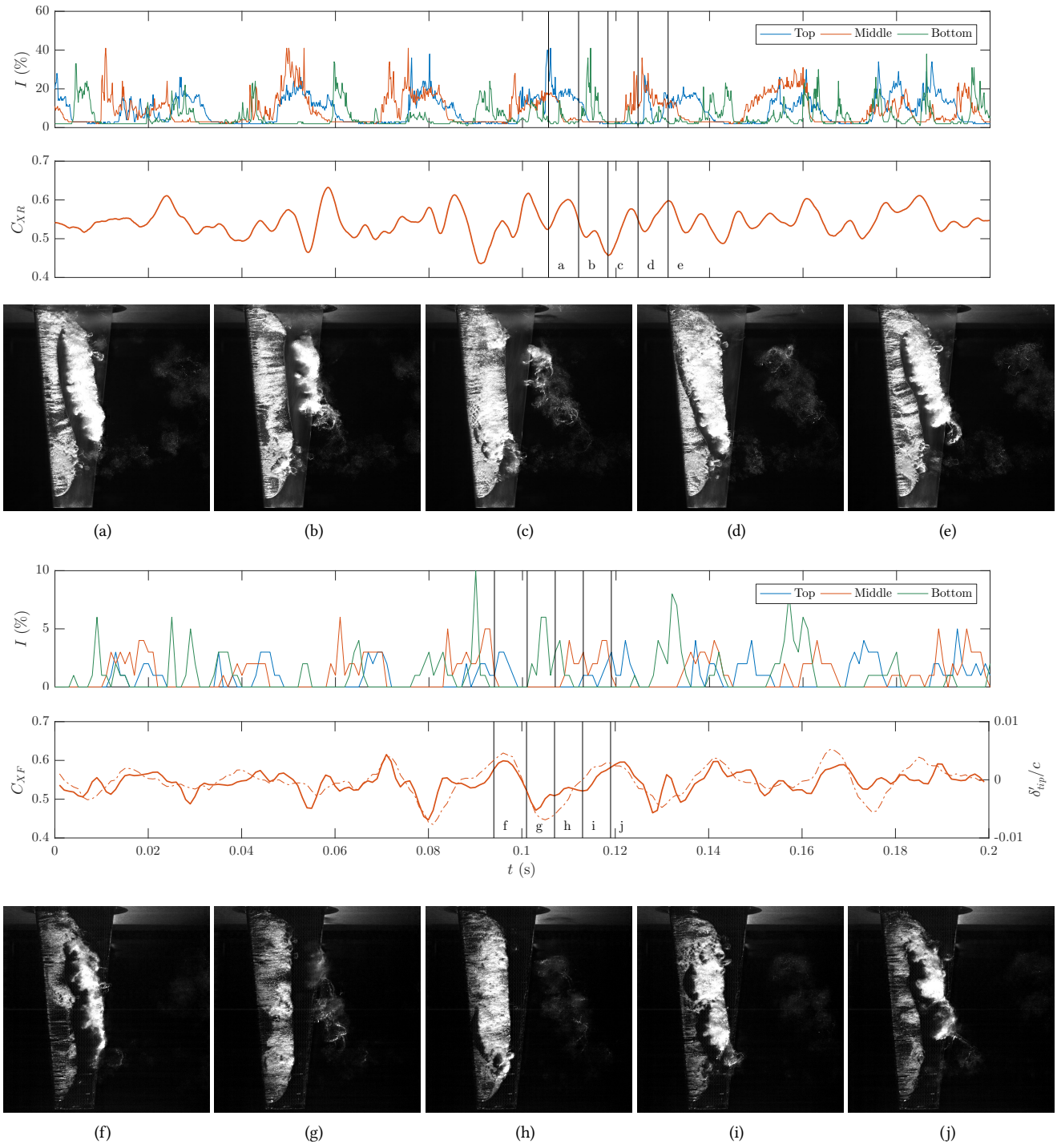


**Figure 4.** Sample time series of normal force coefficient with selected images from high-speed imaging for the rigid hydrofoil (top) and simultaneous normal force coefficient (solid line) and normalized unsteady tip bending displacement (dot-dashed line) with selected images from high-speed imaging for the flexible hydrofoil (bottom) at $\sigma = 0.8$, $Re_c = 0.7 \times 10^6$ and $\alpha = 6°$. The 3 curves of pixel intensity are taken at 75% of the chord for span-wise locations of $0.24s$, $0.47s$ and $0.77s$ from the root.

speed video show one full shedding cycle at the dominant frequency with the first and last frames coinciding with the maximum force of the primary frequency component. For both hydrofoils, the primary frequency corresponds to a full length cavity being shed. The maximum force occurs just after the attached cavity breaks off and a new cavity has just formed. The minimum force coincides with maximum cavity length. Analysing pixel intensity of the rigid hydrofoil we see

a rise, plateau and fall at the middle pixel ($0.47s$) during the shedding cycle shown. The top pixel ($0.24s$) shows similar behaviour and duration but slightly trails the middle pixel intensity in time. The bottom pixel ($0.77s$) exhibits peaks for a much shorter duration compared to the other pixels and primarily occurs when the top and middle pixels are low. These pixel intensity traits suggests there are two shedding modes at the top-middle and the bottom that alternate over time. The flexible hydrofoil shows similar trends but due to low temporal resolution, definitive conclusions cannot be made at this stage.

Comparing the force signals, the rigid hydrofoil exhibits a slightly lower mean $C_X$ to that of the flexible hydrofoil, 0.5406 and 0.5497, respectively. However, the rigid hydrofoil exhibits more unsteadiness with the flexible hydrofoil appearing to almost dampen some of the lower amplitude fluctuations. This is reflected in the $C_X$ RMS values of 0.0354 and 0.0311 for the rigid and flexible hydrofoil, respectively. The unsteady displacement of the flexible hydrofoil is seen to vary significantly over time having a strong correlation with $C_X$ as expected.

## Shedding Mechanisms and Cavity Dynamics

Through analysis of the high speed videos, it is evident that the primary shedding mechanism is the classical re-entrant jet. A typical shedding process can be seen in the space-time plot of the rigid hydrofoil (Figure 5) generated from a line of pixels extracted at a position 100 mm along the span (i.e. at 0.33s). Once the cavity forms, it initially grows at a constant velocity during stage 1. At a certain point ($t \approx 0.01$), the re-entrant jet starts to propagate forward as indicated by a second curve forming in the cavity. At the same instant, the cavity shifts into its second growth phase with a reduced cavity growth speed. As the re-entrant jet approaches the cavity detachment, it starts interacting with the upper surface of the cavity ($t \approx 0.2$). This is indicated by the white streaks from the secondary curve of the re-entrant jet in Figure 5. Shortly after, the jet reaches the cavity detachment, breaking off the attached cavity, forming a cavitation cloud that is then advected downstream. Following cavity break-off, a new cavity forms soon after and the cycle starts again.

At the flow conditions examined here ($Re_c = 0.7 \times 10^6$, $\sigma = 0.8$ and $\alpha = 6°$), the NACA0009 hydrofoil forms a relatively thin cavity, resulting in a thin jet that initially (see stage 1 growth in Figure 5 has insufficient momentum to break through to the cavity detachment point due to friction of the adjacent layers [16, 31]. A sufficiently thin cavity may also have significant interactions between the upper and lower interfaces of the cavity as surface perturbations become predominant leading to small-scale vapour structures being shed instead of a large-scale cloud [19]. This can be seen in chord-wise space-time plots (Figure 6) of several shedding cycles where there is significant variation between each cycle. The interaction of surface perturbations manifest as a rough opaque surface, seen at the top of Figure 6, compared the transparent region shown in Figure 5. Comparison of the rigid and flexible hydrofoils sees that shedding variations

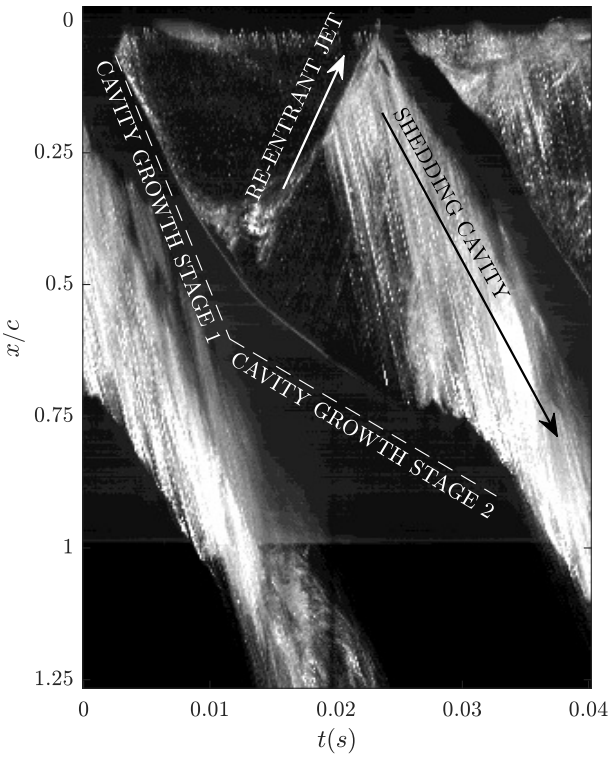


**Figure 5.** Space-time plot of a single shedding cycle of the rigid hydrofoil . showing the key components of the shedding cycle at $\sigma = 0.8$, $Re_c = 0.7 \times 10^6$ and $\alpha = 6°$. The flow direction from top to bottom.

over time exist for both hydrofoils but aren't as severe for the flexible hydrofoil.

The span-wise space-time plots taken 10 mm upstream of mid-chord for both hydrofoils (Figure 7) illustrates how the cloud cavitation varies along the span over time. It is observed that there is significant span-wise variation for both hydrofoils with no uniform (i.e. across the whole span) shedding observed. This complex cavitation behaviour is due to the interaction of multiple effects. This includes span-wise flow disparity over the hydrofoil due to the tapered and swept geometry causing changes in re-entrant jet direction. Additionally, the nature of the vertical mounted hydrofoil results in cavitation number gradient along the span as well as buoyancy effects on the cavities.

A level of consistency is seen in the periodicity of shedding, but the shedding behaviour of each event varies with clear re-entrant jet observed in some, but not in others. Analysis of the rigid hydrofoil reveals the existence of two shedding modes along the span at frequencies of 37 Hz and 50 Hz for the upper and lower parts of the hydrofoil, respectively, calculated from space-time plots. The flexible hydrofoil shows signs of two shedding modes, 37 Hz and 42 Hz, with two crescent cut-outs along the span-wise length of the cavity observed, similar to the rigid hydrofoil. However, the flexible hydrofoils secondary shedding mode at the bottom doesn't appear to have as strong a periodicity. This could be due

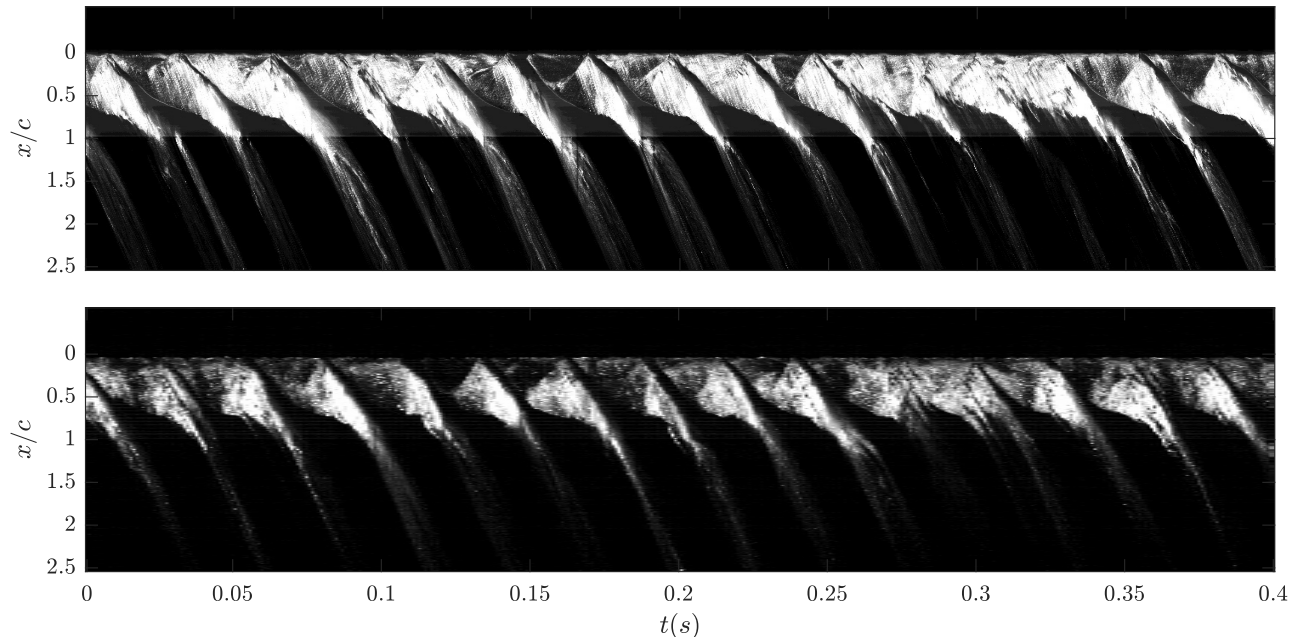


**Figure 6.** Chord-wise space-time plots from high speed images taken 100 mm along the span for the rigid (top) and flexible hydrofoil (bottom) at $\sigma = 0.8$, $Re_c = 0.7 \times 10^6$ and $\alpha = 6°$. The flow direction is top to bottom.

to the force induced tip displacement imposed by the larger shedding cavity from the top interfering with the lower shedding physics. These observations coincide with frequencies present in the $X$ force spectrum (Figure 3) supporting the strong correlation between cavity dynamics and forces.

## CONCLUSIONS

Preliminary results are presented for the effect of FSI on cloud cavitation about a hydrofoil. The normal force, tip bending displacement and cavitation behaviour were compared for a nominally rigid stainless steel and flexible composite NACA0009 hydrofoil at $Re_c = 0.7 \times 10^6$, $\sigma = 0.8$ and $\alpha = 6°$.

The bending deformations of the flexible hydrofoil were seen to dampen some of the higher frequency fluctuations in the normal force measurements while showing a strong correlation between tip displacement and normal force.

A re-entrant jet was identified as the primary shedding mechanism showing changes in growth and jet speed at various stages in the shedding cycle. Due to the thin cavity, surface perturbations were seen to have significant interaction, sometimes resulting in small-scale vapour pockets being shed instead of large-scale cloud cavitation.

The cavitation behaviour is observed to be highly complex due to the 3D nature of the flow leading to significant span-wise flow disparity. Both hydrofoils exhibited fairly consistent periodic shedding but varying behaviour between each event. Two shedding modes appeared to form along the span with either hydrofoil showing two curved regions in the cavity trailing edge typical of a re-entrant jet. This results in two shedding frequencies for either hydrofoil with both having a primary frequency of 37 Hz and secondary frequencies of 50 Hz and 42 Hz for the rigid and flexible hydrofoil, respectively. These differences are attributed to force induced tip bending displacements affecting the cavity dynamics due to changes in the flow field. This is supported by the fact that the observed shedding frequencies matched those present in the $X$ force spectrum.

## ACKNOWLEDGEMENTS

This project was supported by the US Office of Naval Research (Dr.Ki-Han Kim, Program Officer) and ONR Global (Dr.Woei-Min Lin) through NICOP S&T Grant no. N62909-11-1-7013. The authors would like to acknowledge the assistance of Mr Steven Kent and Mr Robert Wrigley from the Australian Maritime College for their essential help with setting up and carrying out the experiments.

## REFERENCES

[1] Y. L. Young. Fluid–structure interaction analysis of flexible composite marine propellers. *Journal of Fluids and Structures*, 24(6):799–818, 2008.

[2] M. R. Motley, Z. Liu, and Y. L. Young. Utilizing fluid–structure interactions to improve energy efficiency of composite marine propellers in spatially varying wake. *Composite Structures*, 90(3):304–313, 2009.

[3] S. R. Turnock and A. M. Wright. Directly coupled fluid structural model of a ship rudder behind a propeller. *Marine Structures*, 13(1):53–72, 2000.

[4] Y. L. Young. Time-dependent hydroelastic analysis of cavitating propulsors. *Journal of Fluids and Structures*, 23(2):269–295, 2007.

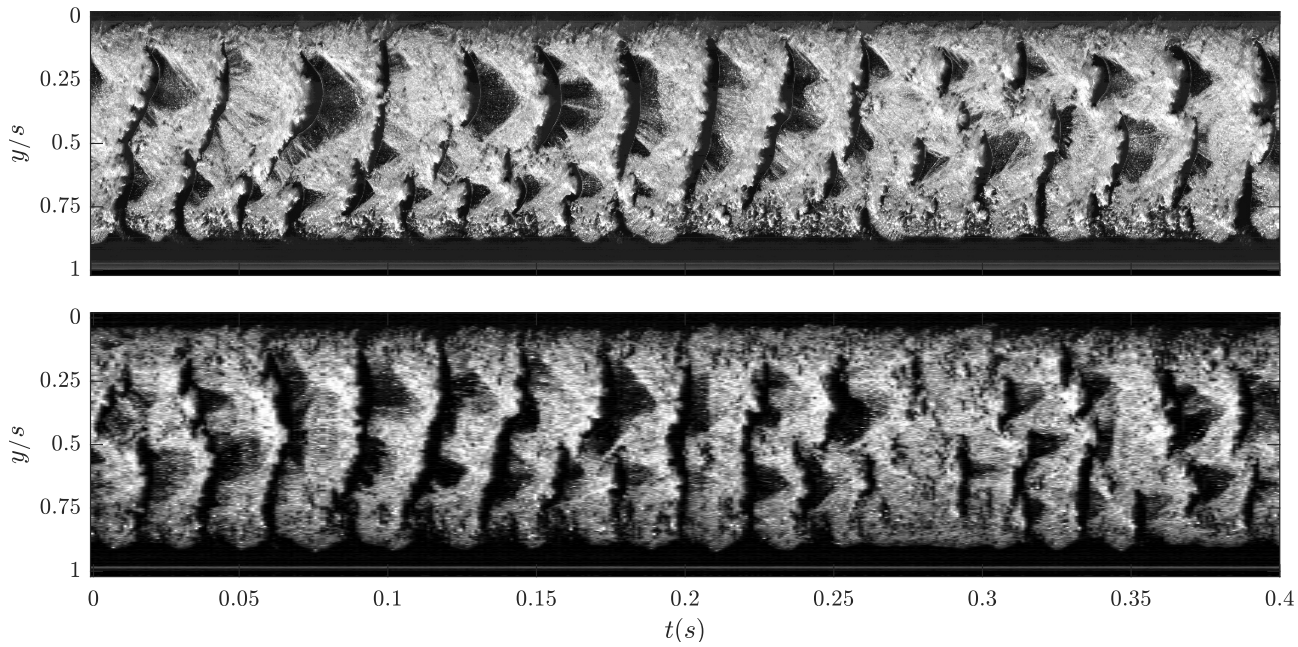


**Figure 7.** Span-wise space-time plots from high speed images 10 mm upstream of the mid-chord for the rigid (top) and flexible hydrofoil (bottom) at $\sigma = 0.8$, $Re_c = 0.7 \times 10^6$ and $\alpha = 6°$. The flow direction is left to right.


[5] D. T. Akcabay and Y. L. Young. Influence of cavitation on the hydroelastic stability of hydrofoils. *Journal of Fluids and Structures*, 49:170–185, 2014.

[6] D. T. Akcabay, E. J. Chae, Y. L. Young, A. Ducoin, and J. A. Astolfi. Cavity induced vibration of flexible hydrofoils. *Journal of Fluids and Structures*, 49(Supplement C):463–484, 2014.

[7] D. T. Akcabay and Y. L. Young. Parametric excitations and lock-in of flexible hydrofoils in two-phase flows. *Journal of Fluids and Structures*, 57:344–356, 2015.

[8] P. Ausoni, M. Farhat, X. Escaler, E. Egusquiza, and F. Avellan. Cavitation influence on von kármán vortex shedding and induced hydrofoil vibrations. *Journal of Fluids Engineering*, 129(8):966–973, 2007.

[9] Q. Wu, B. Huang, G. Wang, and Y. Gao. Experimental and numerical investigation of hydroelastic response of a flexible hydrofoil in cavitating flow. *International Journal of Multiphase Flow*, 74:19–33, 2015.

[10] A. Ducoin, J. A. Astolfi, and J. Sigrist. An experimental analysis of fluid structure interaction on a flexible hydrofoil in various flow regimes including cavitating flow. *European Journal of Mechanics-B/Fluids*, 36:63–74, 2012.

[11] B. W. Pearce, P. A. Brandner, N. Garg, Y. L. Young, A. W. Phillips, and D. B. Clarke. The influence of bend-twist coupling on the dynamic response of cavitating composite hydrofoils. In *5th International Symposium on Marine Propulsors (SMP'17)*, pages 803–813.

[12] R. T. Knapp. Recent investigations of the mechanics of cavitation and cavitation damage. *Transactions of the ASME*, 77:1045–1054, 1955.

[13] C. E. Brennen. The dynamic balances of dissolved air and heat in natural cavity flows. *Journal of Fluid Mechanics*, 37(1):115–127, 1969.

[14] F. Avellan, P. Dupont, and I. L. Ryhming. Generation mechanism and dynamics of cavitation vortices downstream of a fixed leading edge cavity. In *17th Symposium on Naval Hydrodynamics*, pages 1–13, 1988.

[15] S.P. Furness and S. P. Hutton. Experimental and theoretical studies of two-dimensional fixed-type cavities. *Journal of Fluids Engineering*, page 515, 1975.

[16] Q. Le, J. Franc, and J. Michel. Partial cavities: Global behaviour and mean pressure distribution. *Journal of Fluids Engineering*, 115:243–243, 1993.

[17] Y. Kawanami, H. Kato, H. Yamaguchi, M. Tanimura, and Y. Tagaya. Mechanism and control of cloud cavitation. *Journal of Fluids Engineering*, 119(4):788–794, 1997.

[18] B. Stutz and J. L. Reboud. Experiments on unsteady cavitation. *Experiments in Fluids*, 22(3):191–198, 1997.

[19] M. Callenaere, J. Franc, J. Michel, and M. Riondet. The cavitation instability induced by the development of a re-entrant jet. *Journal of Fluid Mechanics*, 444:223–256, 2001.

[20] K. R. Laberteaux and S. L. Ceccio. Partial cavity flows. part 1. cavities forming on models without spanwise variation. *Journal of Fluid Mechanics*, 431:1–41, 2001.

[21] J. K. Jakobsen. On the mechanism of head breakdown in cavitating inducers. *Journal of Basic Engineering*, 86(2):291–305, 1964.

[22] G. E. Reisman, Y. C. Wang, and C. E. Brennen. Observations of shock waves in cloud cavitation. *Journal of Fluid Mechanics*, 355:255–283, 1998.

[23] H. Ganesh, S. A. Mäkiharju, and S. L. Ceccio. Bubbly shock propagation as a mechanism for sheet-to-cloud transition of partial cavities. *Journal of Fluid Mechanics*, 802:37–78, 2016.

[24] KL De Graaf, PA Brandner, and BW Pearce. Spectral content of cloud cavitation about a sphere. *Journal of Fluid Mechanics*, 812, 2017.

[25] E. J. Foeth, C. W. H. Van Doorne, T. Van Terwisga, and B. Wieneke. Time resolved piv and flow visualization of 3d sheet cavitation. *Experiments in Fluids*, 40(4):503–513, 2006.

[26] Y. Kawanami, H. Kato, and H. Yamaguchi. Three-dimensional characteristics of the cavities formed on a two-dimensional hydrofoil. In *Third International Symposium on Cavitation*, volume 1, pages 191–196. Laboratoire des Ecoulements Géophysiques et Industriels, Grenoble, France, 1998.

[27] G. A. Zarruk, P. A. Brandner, B. W. Pearce, and A. W. Phillips. Experimental study of the steady fluid-structure interaction of flexible hydrofoils. *Journal of Fluids and Structures*, 51:326–343, 2014.

[28] D. B. Clarke, D. Butler, B. Crowley, and P. A. Brandner. High-speed full-field deflection measurements on a hydrofoil using digital image correlation. In *30th Symposium on Naval Hydrodynamics*, 2014.

[29] P. A. Brandner, Y. Lecoffre, and G. J. Walker. Design considerations in the development of a modern cavitation tunnel. In *16th Australasian Fluid Mechanics Conference*, pages 630–637, 2007.

[30] Y. L. Young, N. Garg, P. A. Brandner, B. W. Pearce, D. Butler, D. Clarke, and A. W. Phillips. Load-dependent bend-twist coupling effects on the steady-state hydroelastic response of composite hydrofoils. *Composite Structures*, 2017.

[31] P. F. Pelz, T. Keil, and T. F. Groß. The transition from sheet to cloud cavitation. *Journal of Fluid Mechanics*, 817:439–454, 2017.